Electronic Supplementary Material (ESI) for Materials Horizons.


Electronic supplementary information

# Superwettability with antithetic states: Fluid repellency in immiscible liquids

Pingan Zhu[1,2], Tiantian Kong[2,3], Ye Tian[1,2], Xin Tang[1,2], Xiaowei Tian[1,2], Liqiu Wang[1,2,*]

[1] *Department of Mechanical Engineering, the University of Hong Kong, Hong Kong, China*

[2] *HKU-Zhejiang Institute of Research and Innovation (HKU-ZIRI), 311300, Hangzhou, Zhejiang, China*

[3] *Guangdong Key Laboratory for Biomedical Measurements and Ultrasound Imaging, Department of Biomedical Engineering, Shenzhen University, 3688 Nanhai Avenue, Shenzhen, 518060, China*

* Corresponding author. E-mail: lqwang@hku.hk

**Section I. Intrinsic contact angles in reciprocal systems**

Considering the reciprocal systems of liquid A under liquid B and liquid B under liquid A on a smooth surface (Fig. S1a), we characterize the relationship between the intrinsic contact angles $\theta_{\text{A-B}}$ and $\theta_{\text{B-A}}$. Using Young's equation (1) in under-liquid situations, we have the following equations:

$$\cos\theta_{A-B} = \frac{\gamma_{BS} - \gamma_{AS}}{\gamma_{AB}}, \tag{S1}$$

$$\cos\theta_{B-A} = \frac{\gamma_{AS} - \gamma_{BS}}{\gamma_{AB}}, \tag{S2}$$

where $\gamma_{\text{AS}}$, $\gamma_{\text{BS}}$, $\gamma_{\text{AB}}$ denote the solid/liquid A, solid/liquid B, and liquid A/Liquid B interfacial tension, respectively. One can see that $\cos\theta_{A-B} = -\cos\theta_{B-A}$ from equations (S1) and (S2). Since both $\theta_{\text{A-B}}$ and $\theta_{\text{B-A}}$ are in the range of 0 to π, we readily have $\theta_{A-B} + \theta_{B-A} = \pi$ .

**Section II. Cassie and Wenzel state in under-liquid reciprocal systems**

We first consider the liquid A resting on vertical pillar arrays under liquid B (Fig. S1b). From the thermodynamic point of view, the Cassie state is stable if the interfacial energy of Cassie state $E_{\text{C}}$ is lower than that of Wenzel state $E_{\text{W}}$. We have

$$E_C = S_{base}[\gamma_{AB}(1-f_s) + \gamma_{AS}f_s + \gamma_{BS}(r-f_s)] + S_{cap}\gamma_{AB}, \tag{S3}$$

$$E_W = S_{base}\gamma_{AS}r + S_{cap}\gamma_{AB}, \tag{S4}$$

where $S_{\text{base}}$ and $S_{\text{cap}}$ are the surface area of the droplet base and droplet cap, respectively, $f_{\text{s}}$ is the solid fraction of vertical pillars (ratio of pillar area to projected area), $r$ is the roughness ratio of the solid surface (ratio of total solid-surface area to projected area). For a large enough droplet, $S_{\text{cap}}$

keeps invariant in equations (S3) and (S4). If so, we have the energy difference:

$$\Delta E = E_C - E_W = S_{base}[\gamma_{AB}(1-f_s) - \gamma_{AS}(r-f_s) + \gamma_{BS}(r-f_s)]. \quad \text{(S5)}$$

The stable Cassie state yields the $\Delta E < 0$. Therefore, we get the following condition from equation (S5):

$$\frac{\gamma_{AS} - \gamma_{BS}}{\gamma_{AB}} > \frac{1-f_s}{r-f_s}. \quad \text{(S6)}$$

Inserting equation (S1) into (S6), we have

$$\cos\theta_{B-A} > \frac{1-f_s}{r-f_s} \quad \text{(S7)}$$

as the condition for the stable Cassie state of liquid A on vertical pillars under liquid B. Similarly, the condition for stable Cassie state in the reciprocal liquid B under Liquid A system gives,

$$\cos\theta_{A-B} = \frac{\gamma_{BS} - \gamma_{AS}}{\gamma_{AB}} > \frac{1-f_s}{r-f_s}. \quad \text{(S8)}$$

Note that $\cos\theta_{A-B} = -\cos\theta_{B-A}$, indicating that the condition equations (S7) and (S8) cannot be satisfied simultaneously. Therefore, re-entrant structures are introduced to suspend the liquid droplet in the metastable Cassie state (2-3).

**Section III. Filling condition for pillar structure**

When a liquid contact the T-shaped pillar structures, two resisting situations may occur to stop the liquid from spreading: resistance due to the capillary force on vertical pillar walls (Fig. S3a) and due to the pinning at the edge of the cap (Fig. S3b). In the first situation, the resistance comes from the projection of capillary force along the filling direction (Fig. S3c) to be ~$2\gamma H\sin\theta_{e\text{-}a}$ ($\gamma$ the interfacial

tension and $\theta_{e\text{-}a}$ the intrinsic contact angle in the air, and $H$ the pillar height), and the driven force originates from the capillary force on the bottom of the surface (Fig. S3d) where the projection along the filling direction gives $\sim\gamma L\cos\theta_{e\text{-}a}$ ($L$ the pillar spacing). Balancing the two forces yields the condition for overcoming the resistance on vertical walls:

$$\theta_{e\text{-}a} < \arctan(L/2H). \tag{S9}$$

To overcome pinning resistance in the second situation (Fig. S3b), the liquid front can spread either up along the cap or laterally to wet the next row of pillars (also known as wicking (4)). The condition for spreading up along the cap is $\frac{\pi}{2} - \theta_{e-a} > \theta_{e-a}$, yielding

$$\theta_{e-a} < \pi / 4 . \tag{S10}$$

The wicking condition gives $\tan\theta_{e\text{-}a} < H/L$, where $\theta_{e\text{-}a}$ should satisfy:

$$\theta_{e-a} < \arctan(H / L) . \tag{S11}$$

Therefore, depinning from the edge of the cap takes place when one of the conditions (S10) and (S11) is satisfied, as shown in Fig. S3e, which is

$$\theta_{e-a} < \max[\pi / 4, \arctan(H / L)] . \tag{S12}$$

To realize spontaneous filling, both of the resisting situations should be overcome, such that equations (S9) and (S12) must be satisfied simultaneously, as shown in Fig. S3f. Therefore, the filling condition for pillar structure gives:

$$\theta_{e\text{-}a} < \arctan(L/2H) \text{ when } L/H < 2 \text{ and } \theta_{e\text{-}a} < 45° \text{ when } L/H > 2. \tag{S13}$$

**Section IV. Breakthrough pressure for square pillar arrays and cages**

The breakthrough pressure can be scaled by a force balance between the pressure inside the liquid and the surface tension (2): $P_{break}S_{int} = \gamma L_{tot}\sin(\theta_e - \varphi)$ where $S_{\text{int}}$ is the interfacial area, $L_{\text{tot}}$ is the total length of the three-phase contact line, $\theta_{\text{e}}$ is the equilibrium contact angle, and $\varphi$ is the minimum geometric angle. For periodic structures, the breakthrough pressure can be estimated based on the calculation of $S_{\text{int}}$ and $L_{\text{tot}}$ for one unit cell. For square pillar arrays (as shown in the left of Fig. 2B), $S_{int} = L^2\left(1 - f_s\right)$, $f_s = \dfrac{\pi D^2}{4L^2}$, $L_{tot} = \pi D$. Therefore, the breakthrough pressure for square pillar arrays is

$$P_p = \frac{2\gamma\sqrt{f_s\pi}}{L(1-f_s)}\sin(\theta_e - \varphi). \tag{S14}$$

For square cage structures (shown in the right of Fig. 2B), $S_{int} = L^2\left(1 - f_s\right)$, $f_s = 1 - \left(\dfrac{L-2W}{L}\right)^2$, $L_{tot} = 4(L-2W)$ where $W$ is the semi-width of the cage arris. As such, the breakthrough pressure for square cage is

$$P_c = \frac{4\gamma}{L\sqrt{1-f_s}}\sin(\theta_e - \varphi). \tag{S15}$$

**Section V. Rim length for triangular, square, and hexagonal cages**

If the rim length of one side of the triangular cage structure (as shown in Fig. 2E) is $l_{\text{t}}$, we readily have $\dfrac{\sqrt{3}}{4}l_t^2 = S(1-f_s)$ and the rim length per unit area gives $L_{rt} = \dfrac{3l_t}{S} = \dfrac{6}{\sqrt[4]{3}}\sqrt{\dfrac{1-f_{\text{s}}}{S}}$. Similarly, if the rim length for the square cage structure is $l_{\text{s}}$, we have $l_s^2 = S(1-f_s)$ and the rim length per unit

area gives $L_{rs} = \frac{4l_s}{S} = 4\sqrt{\frac{1-f_s}{S}}$. For hexagonal cage structure with rim length for one side of $l_h$, it gives $\frac{3}{2}\sqrt{3}l_h^2 = S(1-f_s)$ and $L_{rh} = \frac{6l_h}{S} = \frac{6\sqrt[4]{4}}{\sqrt[4]{27}}\sqrt{\frac{1-f_s}{S}}$.

**Section VI. Estimate of surface roughness *r***

Surface roughness *r* is defined as the actual surface area divided by the projected surface area. For the hexagonal micro-cage surface (Fig. 2F and Fig. S7), the projected surface area of one unit cell is $S_{pro} = 2\sqrt{3}R_c^2$, and the actual surface area $S_{act} = S_{rim} + S_{pill} + S_{pro}$ where $S_{rim}$ is the surface area of the top hexagonal rim and $S_{pill}$ is the surface area of the supporting pillars. Since the rim has upper-side and lower-side faces, $S_{rim} = 2 \times 2\sqrt{3}(R_c^2 - R_o^2) = 4\sqrt{3}(R_c^2 - R_o^2)$. One hexagonal cell has six pillars, but each pillar is shared by three adjacent hexagonal cells. As such, the surface area of the pillar is $S_{pill} = 6 \times \frac{1}{3} \times 2\pi r_{pill} h_{pill} = 4\pi r_{pill} h_{pill}$ where $r_{pill}$ and $h_{pill}$ are the radius and height of the pillar, respectively. $h_{pill}$ roughly equals the height of the micro-cage surface, estimated by the mass conservation of the oil droplet template, $\frac{4}{3}\pi R_c^3 = 2\sqrt{3}R_c^2 h_{pill}$ (the left-hand-side represents the volume of a spherical oil droplet and the right-hand-side stands for the volume of the hexagonal-prism oil template after shape deformation), to be $h_{pill} = \frac{2\sqrt{3}}{9}\pi R_c$. The radius of the pillar is estimated to be (Fig. S7) $r_{pill} = \frac{2\sqrt{3}}{3}(R_c - R_o)$. Then the surface area of the pillar is $S_{pill} = 4\pi r_{pill} h_{pill} = \frac{16}{9}\pi^2(R_c^2 - R_c R_o)$. The surface roughness *r* is thus: $r = \frac{S_{act}}{S_{pro}} = \frac{S_{rim} + S_{pill} + S_{pro}}{S_{pro}} = 1 + 2[1 - (\frac{R_o}{R_c})^2] + \frac{8\sqrt{3}}{27}\pi^2(1 - \frac{R_o}{R_c})$. For the micro-cage surface shown in Fig. 2F that $R_o$ = 74.05 μm and $R_c$ = 77.85 μm, so that surface roughness is $r$ = 1.4377.

**Section VII. Breakthrough pressure for hexagonal micro-cage surface**

We still use the equation $P_{break}S_{int} = \gamma L_{tot}\sin(\theta_e - \varphi)$ to scale the breakthrough pressure for the hexagonal micro-cage surface, $P_{\text{break}}$. In this case, $S_{int} = 2\sqrt{3}R_c^2\left(1-f_s\right)$ , $f_s = 1-(\frac{R_o}{R_c})^2$ , $L_{tot} = 4\sqrt{3}R_o$. As such, the breakthrough pressure leads to $P_{\text{break}} = \frac{2\gamma\sin(\theta_{\text{e-l}} - \varphi)}{R_{\text{c}}\sqrt{1-f_{\text{s}}}}$ where $\theta_{\text{e-l}}$ is the under-liquid intrinsic contact angle. Here, the minimum geometric angle $\varphi$ = 0° for the micro-cage surface. When $\theta_{\text{e-l}} \geq 90°$ we have $P_{\text{break}} = \frac{2\gamma}{R_{\text{c}}\sqrt{1-f_{\text{s}}}}$. As a result, we obtain the expression for breakthrough pressure in the form of $P_{break} = \frac{2\gamma}{R_{\text{c}}\sqrt{1-f_{\text{s}}}}F(\theta_{\text{e-l}})$ where $F(\theta_{\text{e-l}}) = \sin\theta_{\text{e-l}}$ if $\theta_{\text{e-l}} < 90º$, and $F(\theta_{\text{e-l}}) = 1$ if $\theta_{\text{e-l}} \geq 90º$.

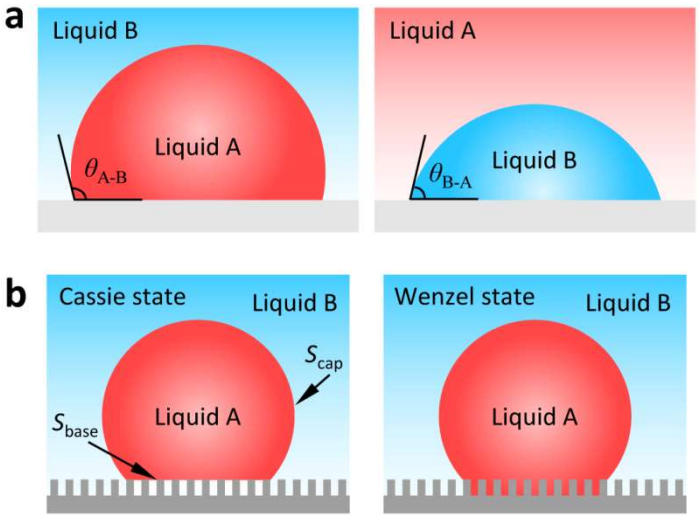


**Fig. S1. Solid-liquid interactions in under-liquid situations.** (a) Intrinsic contact angles in the reciprocal liquid A under liquid B and liquid B under liquid A systems. (b) Cassie and Wenzel state for the liquid A on a roughed surface under the liquid B.

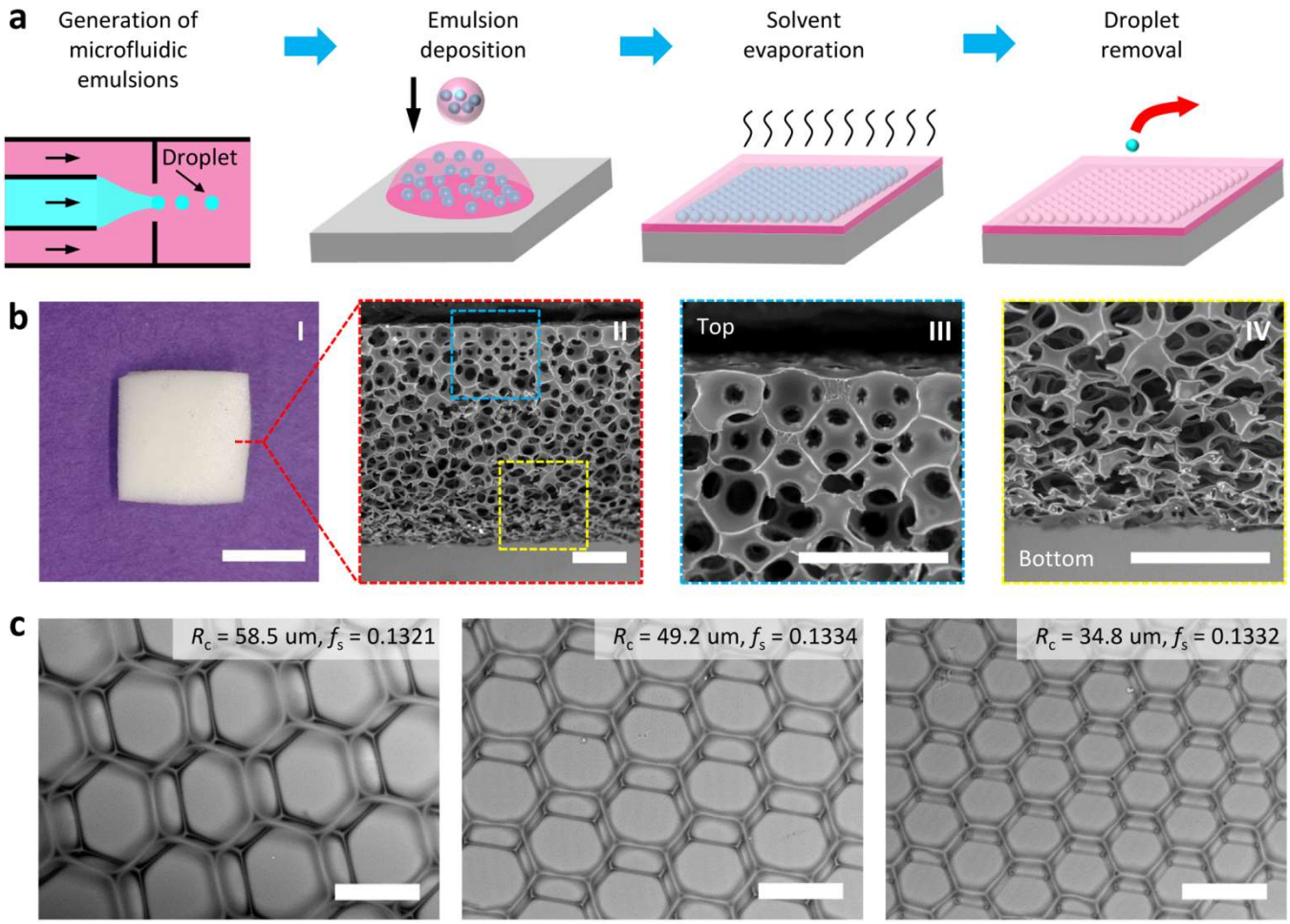


**Fig. S2. Porous surfaces fabricated by the microfluidic emulsion templating method.** (a) Schematic of the four-step fabrication process (not to scale): emulsion generation, emulsion deposition, solvent deposition, and droplet removal. (b) Multi-layered porous membrane (I) whose top and bottom sides are anisotropic in the pore structures (II-IV). Scale bars, I, 5 mm; II-IV, 300 μm. (c) Monolayer micro-cage surface. The unit cell size ($R_c$) can be varied while the solid fraction ($f_s$) is kept as constant, denoting that $R_c$ and $f_s$ can be independently controlled. Scale bar, 100 μm.

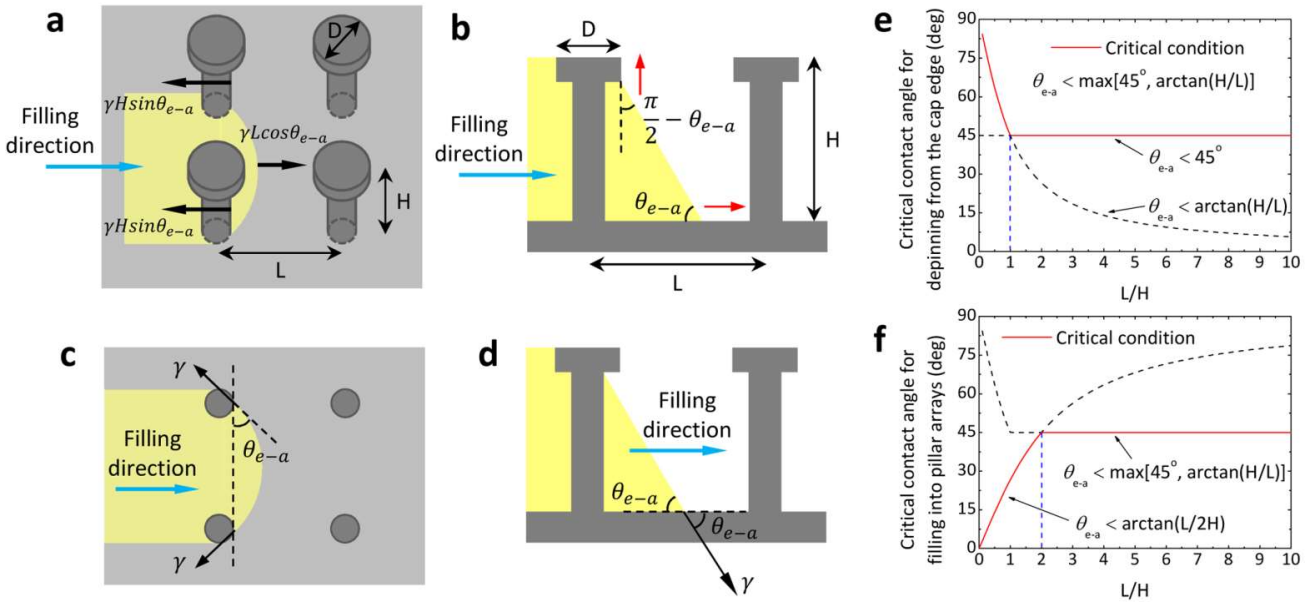


**Fig. S3. Wetting the square pillar arrays from the lateral side.** (a) Spontaneous filling of a liquid resisted by the capillary forces from the vertical pillar walls, as the first resisting situation. (b) Contact line pinning at the edge of the cap as the second resisting situation. (c) Schematic showing the resistance from pillar walls in the first situation (top view). (d) Schematic showing the driven capillary force in the first situation (side view). (e) Critical intrinsic contact angle as the condition for the contact line depinning from the cap edge (solid red line). (f) Condition for the spontaneous filling of a liquid into the square pillar arrays (solid red line).

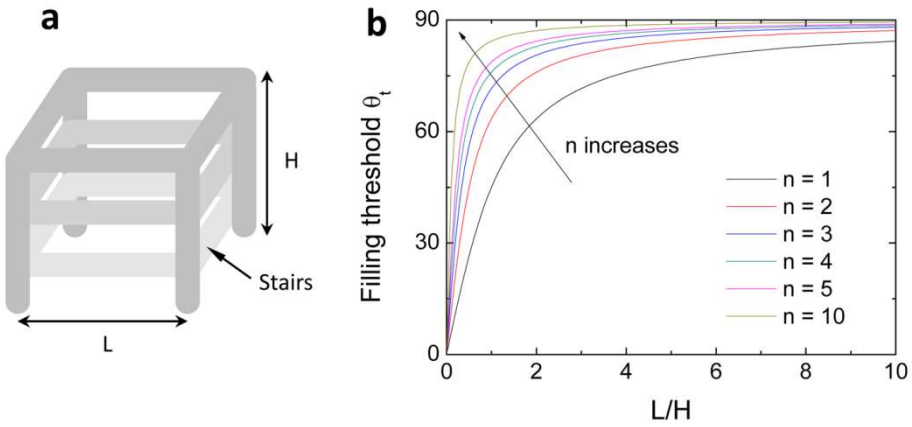


**Fig. S4. Influence of the number of stairs *n* on the filling threshold.** (a) Schematic showing an example of cage structure with 3 layers of stairs ($n$ = 3). (b) The filling threshold $\theta_c$ increasing with the number of stairs $n$, $\theta_c = \arctan(nL/H)$.

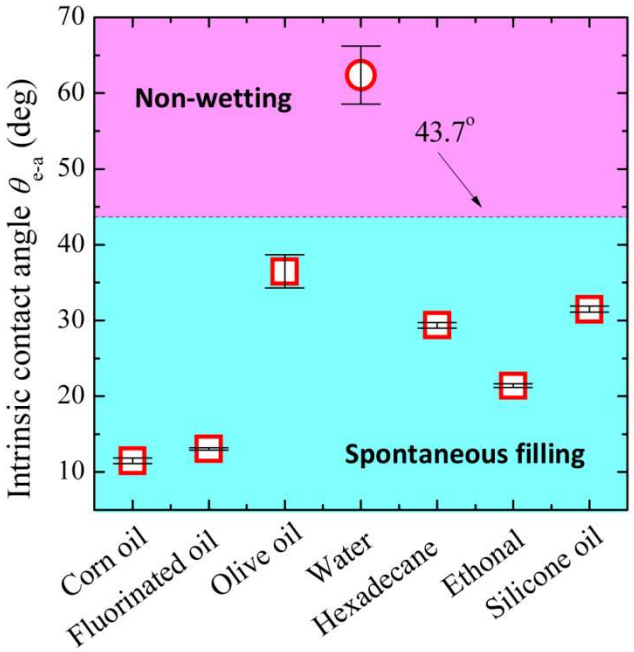


**Fig. S5. The condition for spontaneous filling of liquids into the fabricated hexagonal cage surface.** The dashed line gives the condition of $\theta_{e\text{-}a} = 43.7°$ as the theoretical prediction. The symbols denote the experimental measurements, where square represents spontaneous filling and circle stands for non-wetting. The experimental results for liquids used agree well with the theoretical calculation.

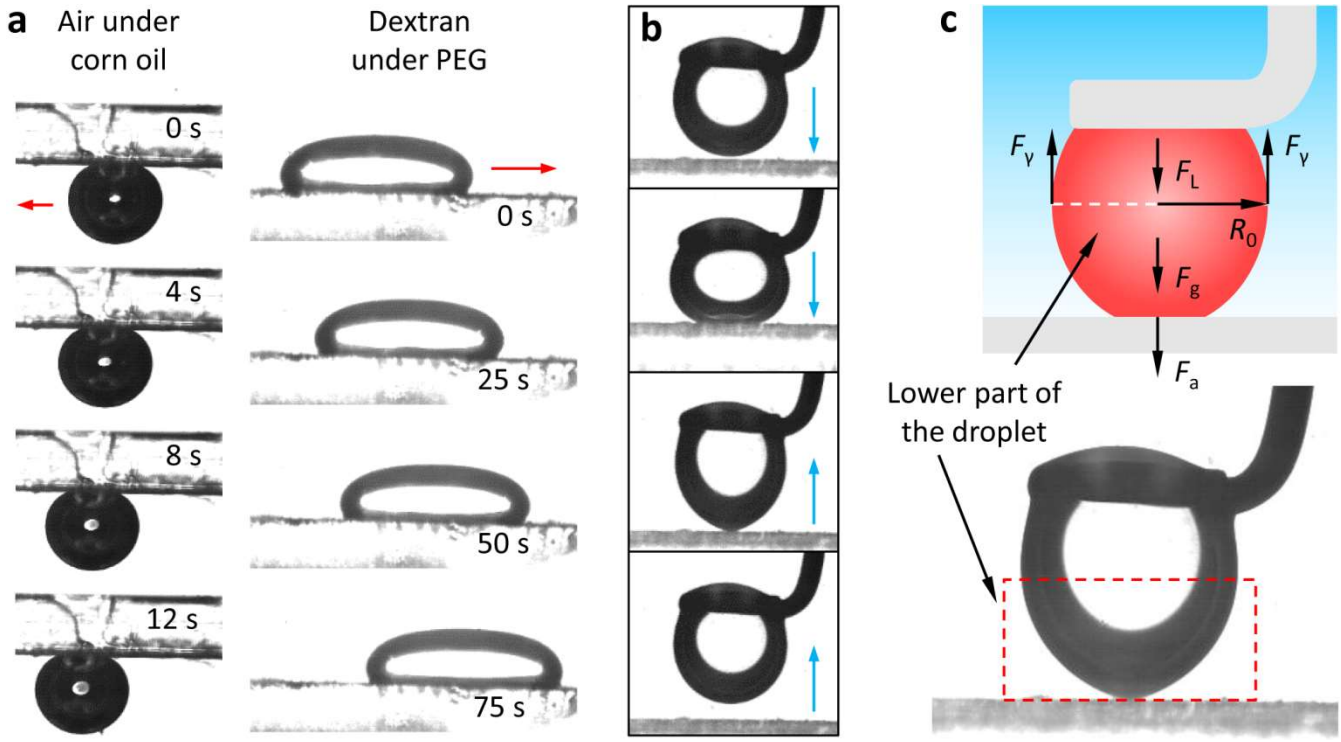


**Fig. S6. Measurement of adhesion**. (a) Air bubble sliding under corn oil (the left row, surface tilted by ~1.1º) and dextran droplet rolling off under polyethylene glycol (PEG) aqueous solution (the right row, surface tilted by ~1.4º), showing very low adhesive forces. (b) Measurement of adhesion by compressing and relaxing the droplet on the horizontally placed surface. (c) Schematic (upper) and snapshot (lower) of force balance analysis on the lower part of the droplet.

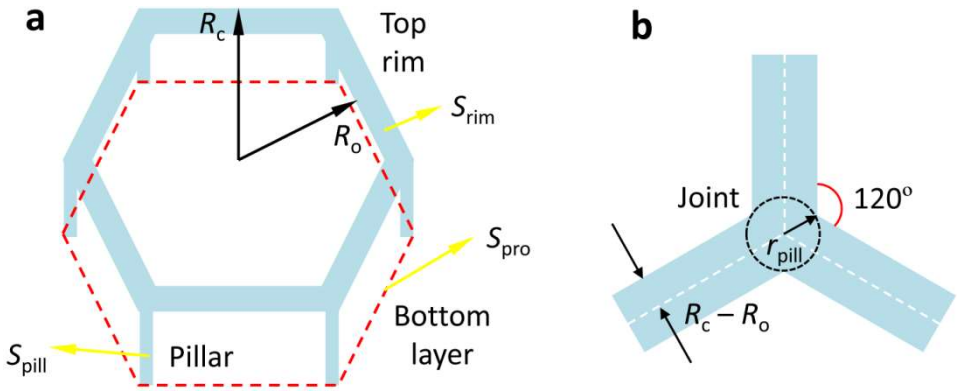


**Fig. S7. The surface roughness of the hexagonal micro-cage structure**. (a) Schematic of a unit hexagonal cell. The actual surface area is the sum of the surface area of the top rim, $S_{rim}$, supporting pillar, $S_{pill}$, and bottom projection, $S_{pro}$. (b) Estimate of the pillar radius $r_{pill}$. $r_{pill}$ is evaluated to be the in-circle radius of the joint of the three adjacent unit cells.

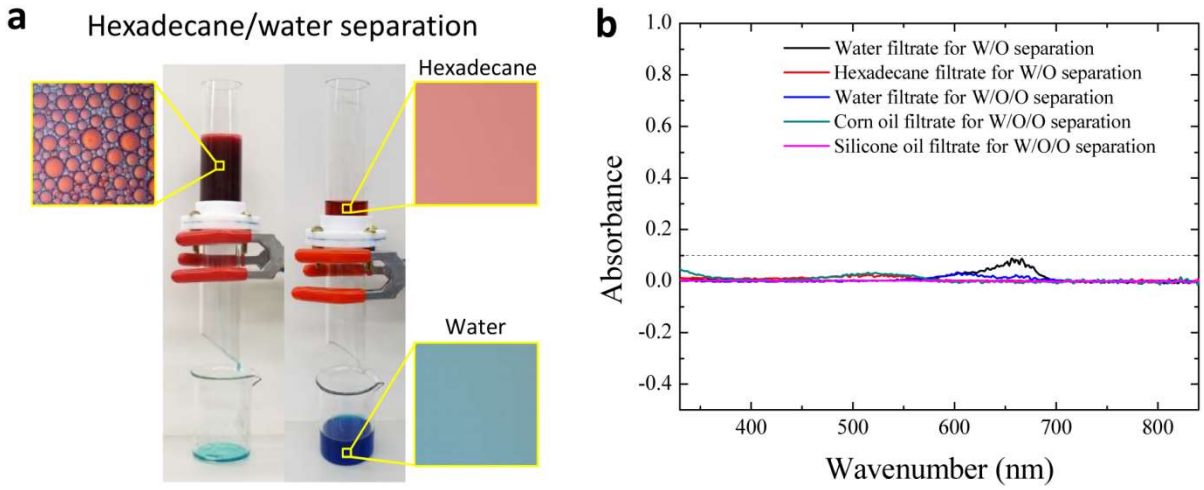


**Fig. S8. Separation of multi-component liquids using the hexagonal micro-cage surface**. (a) Separation of a hexadecane-in-water emulsion. Hexadecane is dyed red using Oil Red O and water is dyed using Methylene Blue. (b) Ultraviolet-visible (UV-Vis) absorption spectra for liquid filtrates in (**a**) and Fig. 4a. The absorption spectra were measured using the pure liquid as a blank for each filtrate. The relative absorbance is around zero (fluctuation amplitude <0.1 for all filtrates), indicating highly-purified filtrates.

**Table S1. Intrinsic contact angles for all test systems**

| System | Intrinsic contact angle $\theta_{e\text{-}l}$ (°) |
|---|---|
| air under corn oil | 138.8 |
| air under ethanol | 158.6 |
| air under hexadecane | 150.6 |
| air under olive oil | 143.5 |
| air under silicone oil | 148.5 |
| air under water | 117.6 |
| corn oil under silicone oil | 43.2 |
| corn oil underwater | 111.9 |
| decanol underwater | 69.5 |
| ethanol under corn oil | 73.6 |
| fluorinated oil underwater | 65.5 |
| hexadecane underwater | 112.6 |
| olive oil underwater | 91.2 |
| silicone oil under corn oil | 136.8 |
| silicone oil underwater | 111.3 |
| soybean oil underwater | 98.1 |
| toluene underwater | 59.7 |
| water under corn oil | 64.5 |
| water under decanol | 110.5 |
| water under hexadecane | 67.4 |
| water under silicone oil | 100.3 |

**Supplementary References**


1. Young T (1805) An essay on the cohesion of fluids. *Philos Trans R Soc London* 95:65-87.

2. Tuteja A, Choi W, Mabry JM, McKinley GH, & Cohen RE (2008) Robust omniphobic surfaces. *Proc Natl Acad Sci USA* 105:18200-18205.

3. Tian X, Jokinen V, Li J, Sainio J, & Ras RHA (2016) Unusual dual superlyophobic surfaces in oil–water systems: the design principles. *Adv Mater* 28:10652-10658.

4. Semprebon C, Forsberg P, Priest C, & Brinkmann M (2014) Pinning and wicking in regular pillar arrays. *Soft Matter* 10:5739-5748.

**Supplementary Movies**

**Movie S1: Non-wetting top surface of the multi-layered porous membrane**

A 10-μL corn oil droplet rests on the top surface of the porous membrane. The video is played in real time.

**Movie S2: Wicking at the bottom of the multi-layered porous membrane**

A 10-μL corn oil droplet penetrates into the porous membrane from the bottom side, giving rise to an apparent contact angle of 0°. The video is played in real time.

**Movie S3: Air bubble sliding under silicone oil**

An air bubble slides on the micro-cage surface tilted by 1.1º under silicone oil. The video is played 2 times slower than real time.

**Movie S4: Dextran droplet sliding under PEG solution**

A dextran droplet slides on the micro-cage surface tilted by 1.4º under PEG aqueous solution. The video is played x10 faster than real time.

**Movie S5: Underoil water harvesting**

The water-infused micro-cage surface selectively captures the water droplet from the vapor-water hybrid droplet while repels the vapor bubble away. The video is played x16 slower than real time.

**Movie S6: Water droplet sticks on the Janus-infused micro-cage surface**

The micro-cage surface is immersed in corn oil and infused with corn oil and water at its upper and lower part, respectively. A water droplet sticks at the lower water-infused part when sliding down the inclined surface. The video is played in real time.

**Movie S7: Silicone oil droplet slides down the Janus-infused micro-cage surface**

The micro-cage surface is immersed in corn oil and infused with corn oil and water at its upper and lower part, respectively. A silicone oil droplet slides along the inclined surface to the bottom. The video is played in real time.

**Movie S8: Breakup of a water/silicon-oil Janus droplet on the Janus-infused micro-cage surface**

The micro-cage surface is immersed in corn oil and infused with corn oil and water at its upper and lower part, respectively. A water/silicone-oil Janus droplet breaks up into individual water and silicone oil droplets and sorted by the surface. The video is played x4 faster than real time.